



Anisotropic scaling of tectonic stylolites: A fossilized signature of the stress field?

Marcus Ebner,^{1,2} Renaud Toussaint,^{3,4} Jean Schmittbuhl,^{3,4} Daniel Koehn,¹ and Paul Bons⁵

Received 26 May 2009; revised 15 October 2009; accepted 13 January 2010; published 19 June 2010.

[1] Vertical stylolites are pressure solution features, which are considered to be caused by horizontal tectonic loading, with the largest principal compressive stress being (sub-) parallel to the Earth's surface. In the present study we analyze the roughness of such tectonic stylolites from two tectonic settings in southern Germany and northeastern Spain, aiming to investigate their scaling properties with respect to the stress during formation. High-resolution laser profilometry was carried out on opened stylolite surfaces of nine samples. These data sets were then analyzed using one- and two-dimensional Fourier power spectral approaches. We found that tectonic stylolites show two self-affine scaling regimes separated by a distinct crossover length (L), as known for bedding parallel stylolites. In addition, tectonic stylolites exhibit a clear in-plane scaling anisotropy that modifies L . Since the largest and smallest crossover lengths are oriented with the sample vertical and horizontal directions (i.e., σ_2 and σ_3) and L is a function of the stress field during formation as analytically predicted, we conclude that the scaling anisotropy of tectonic stylolites is possibly a function of the stress field. Knowledge of this crossover-length anisotropy would enable the reconstruction of the full three-dimensional stress tensor if independent constraints of the depth of formation can be obtained.

Citation: Ebner, M., R. Toussaint, J. Schmittbuhl, D. Koehn, and P. Bons (2010), Anisotropic scaling of tectonic stylolites: A fossilized signature of the stress field?, *J. Geophys. Res.*, *115*, B06403, doi:10.1029/2009JB006649.

1. Introduction

[2] The intriguing variety of pressure solution features and its widespread occurrence in monomineralic rock types have provoked continuous interest in and attention to various geoscience disciplines over the past decades [Tada and Siever, 1989]. One of the most prominent and complex pressure solution features is stylolites, which are rough dissolution interfaces that are found in a large variety of sedimentary rocks [Buxton and Sibley, 1981; Dunnington, 1954; Heald, 1955; Park and Schot, 1968; Railsback, 1993; Rutter, 1983; Stockdale, 1922; Tada and Siever, 1989]. Until recently stylolite morphology has been described qualitatively by the use of a descriptive terminology that groups stylolites into generic classes. One classification uses the orientation of the stylolite plane relative to bedding. Bedding parallel stylolites are supposed to have formed owing to the layer-normal overburden pressure, while tectonic stresses cause the formation of stylolites oblique or per-

pendicular to bedding [Park and Schot, 1968; Railsback and Andrews, 1995]. The second classification is based on the orientation of the stylolite teeth relative to the stylolite plane. Here the term “stylolite” is used for teeth at a high angle to the plane, and the term “slickolite” is used for dissolution surfaces where the teeth are distinctly oblique to the dissolution plane [Bretz, 1940; Gratier et al., 2005; Simon, 2007]. Finally, the shape of the characteristic teeth-like asperities and spikes along the interface has been used to characterize stylolites [Guzzetta, 1984; Park and Schot, 1968].

[3] More recently, stylolites have been subjected to more rigorous quantitative analyses to characterize the roughness of the stylolite surface [Brouste et al., 2007; Drummond and Sexton, 1998; Ebner et al., 2009a–2009b; Gratier et al., 2005; Karcz and Scholz, 2003; Koehn et al., 2007; Renard et al., 2004; Schmittbuhl et al., 2004]. It was demonstrated that the one-dimensional (1-D) stylolite roughness obeys a fractal scaling invariance [Drummond and Sexton, 1998; Karcz and Scholz, 2003]. Investigation of the rough interface of opened stylolite surfaces by means of laser profilometry revealed that the stylolite morphology shows two self-affine scaling regimes with two distinct roughness exponents on their respective scales, which are separated by a characteristic crossover length at the millimeter scale [Renard et al., 2004; Schmittbuhl et al., 2004] for bedding parallel stylolites. Self-affine surfaces define a group of fractals that remain statistically unchanged by the transform, $\Delta x \rightarrow b \times \Delta x$, $\Delta y \rightarrow b \times \Delta y$, $\Delta z \rightarrow b^H \times \Delta z$, where b is a transformation factor that can take any real value and H is

¹Tectonophysics, Institute of Geosciences, Johannes Gutenberg University, Mainz, Germany.

²Now at Geological Survey of Austria, Vienna, Austria.

³EOST, University of Strasbourg, Strasbourg, France.

⁴Also at Institut de Physique du Globe de Strasbourg, UMR CNRS 7516, Strasbourg, France.

⁵Institute for Geosciences, Eberhard Karls University Tübingen, Tübingen, Germany.

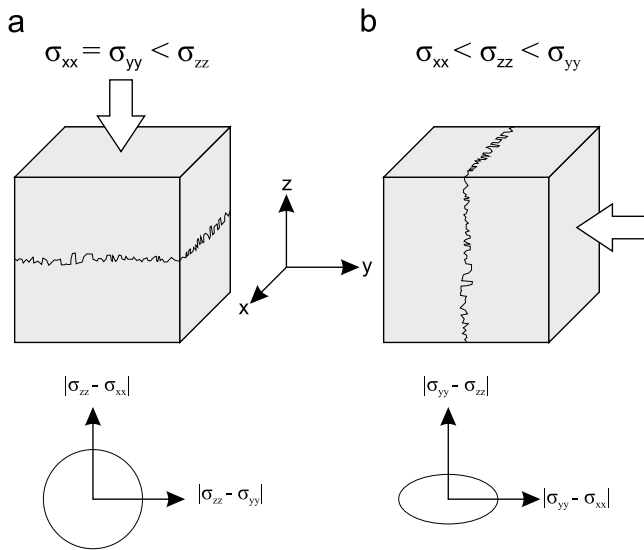


Figure 1. Schematic drawing of the formation stress state for (a) bedding parallel and (b) tectonic stylolites. The largest compressive stress direction (σ_1) is indicated by the white arrow. Below the sketch map an idealized graph of the in-plane differential stress is plotted as a function of the orientation within the stylolite plane. For bedding parallel stylolites (a) the horizontal normal stresses are equal and thus the differential stress is equal in every direction. For tectonic stylolites (b) the in-plane normal stresses are dissimilar and σ_{zz} is generally larger than σ_{xx} . Thus the in-plane differential stress scales inversely with the magnitudes of the σ_{xx} and σ_{zz} directions, having a maximum along the x axis.

the Hurst or roughness exponent [Barabasi and Stanley, 1995], which is a quantitative measure of the roughness of the signal.

[4] Analytical and numerical investigations have demonstrated that the growth of the stylolite roughness is induced by heterogeneities in the host rock that pin the interface and is slowed down by two stabilizing forces, the elastic and surface energies. The elastic energy dominates on larger scales and is represented by a small roughness exponent of 0.3 to 0.5, whereas the surface energy is dominant on small scales, with a roughness exponent of about 1 [Koehn et al., 2007; Renard et al., 2004; Schmittbuhl et al., 2004]. The characteristic crossover length (L) that separates these two scaling regimes is a function of the principal normal stress [Renard et al., 2004; Schmittbuhl et al., 2004] on the interface of a bedding parallel stylolite. These analytical predictions were successfully tested by Ebner et al. [2009b], who demonstrated, on a set of 13 bedding parallel stylolites from varying stratigraphic depths of a cretaceous succession, that this crossover length decreases with increasing depth (and normal stress) and thus exhibits the analytically predicted behavior. The 1-D scaling of stylolites with two self-affine scaling invariance regimes can be described as the height difference h of points along the surface separated by a distance Δx as [Ebner et al., 2009b]

$$h(\Delta x) \approx A \Delta x^{H_S} g(\Delta x/L) \text{ with } g(u) = \begin{cases} u^0 & \text{if } u \ll 1, \\ u^{H_L - H_S} & \text{if } u \gg 1, \end{cases} \quad (1)$$

where A is a scaling factor, g is a scaling function, and u is the ratio $\Delta x/L$, with L being the crossover length. H_S and H_L correspond to the roughness exponents for small and large scales, respectively. Numerical simulations also demonstrate that the crossover length is very robust with regard to the kind and amount of quenched noise (heterogeneities initially present) in the rock [Ebner et al., 2009a]. Hence, the use of bedding parallel stylolites as a quantitative stress gauge under the assumption of uniaxial strain (zero horizontal displacement) seems to be verified. Investigations of the surface morphology of bedding parallel stylolites showed that their scaling is isotropic within the plane defined by the stylolite [Renard et al., 2004; Schmittbuhl et al., 2004]. This implies that any arbitrary section through the stylolite interface that contains the principal stress direction (i.e., normal to the plane) fully characterizes the complex self-affine roughness of bedding parallel stylolites. A second mechanism claimed to be responsible for the formation of the characteristic roughness is a stress-induced roughening instability along an initially flat solid-solid interface [Angheluta et al., 2008] or a solid-fluid-solid interface [Bonnetier et al., 2009]. In both cases the instability is triggered by elastic stresses acting normal on the interface.

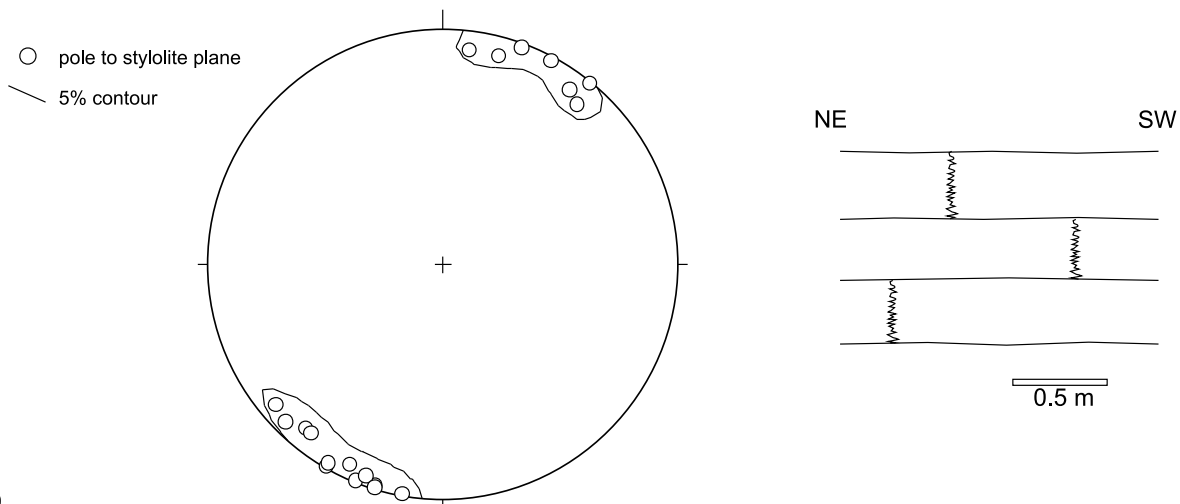
[5] Up to now no study has quantitatively investigated the 3-D topography of tectonic stylolites that formed owing to (sub-)horizontal compression resulting in a vertical stylolite plane. Tectonic stylolites differ in two major characteristics from bedding parallel stylolites. First, the stress field during the formation of tectonic stylolites is nonisotropic, that is, the in-plane normal stresses differ (i.e., $\sigma_{zz} > \sigma_{xx}$), whereas bedding parallel stylolites often have equal in-plane normal stresses $\sigma_{xx} = \sigma_{yy}$ (Figure 1). This implies that the scaling of tectonic stylolites is not invariant within the plane, since the crossover length should scale with the (nonisotropic) stress field as shown analytically [Schmittbuhl et al., 2004]. A second common feature of tectonic stylolites are oblique/tilted teeth with respect to the mean stylolite plane due to overprinting of pre-existing planes of anisotropy such as joints, bedding planes, and other interfaces. Tilting of the teeth with respect to the stylolite plane also influences the morphology because it leads to the dominance of long grooves and ridges [Simon, 2007]. These features could lead to an anisotropic scaling of the stylolite interface in addition to variations of the in-plane stresses.

[6] The present study investigates such tectonic stylolites that formed in a vertical orientation. We mainly concentrate on the influence of (i) the orientation of the dissolution surface with respect to the displacement direction and (ii) the formation stress on the scaling properties of natural stylolites in limestones. To accomplish this task we use laser profilometry data on opened interfaces of tectonic stylolites from flat-lying Jurassic limestones of the Swabian Alb in southern Germany and from a Tertiary fold and thrust belt of the Iberian Chain of northeastern Spain.

2. Geological Setting

[7] In this section we give a brief introduction of the investigated field areas in southern Germany and northeastern Spain, which both expose upper Jurassic limestones. The Swabian Alb of southern Germany forms a region of flat-lying, mainly marine Jurassic deposits [Geyer and

a



b

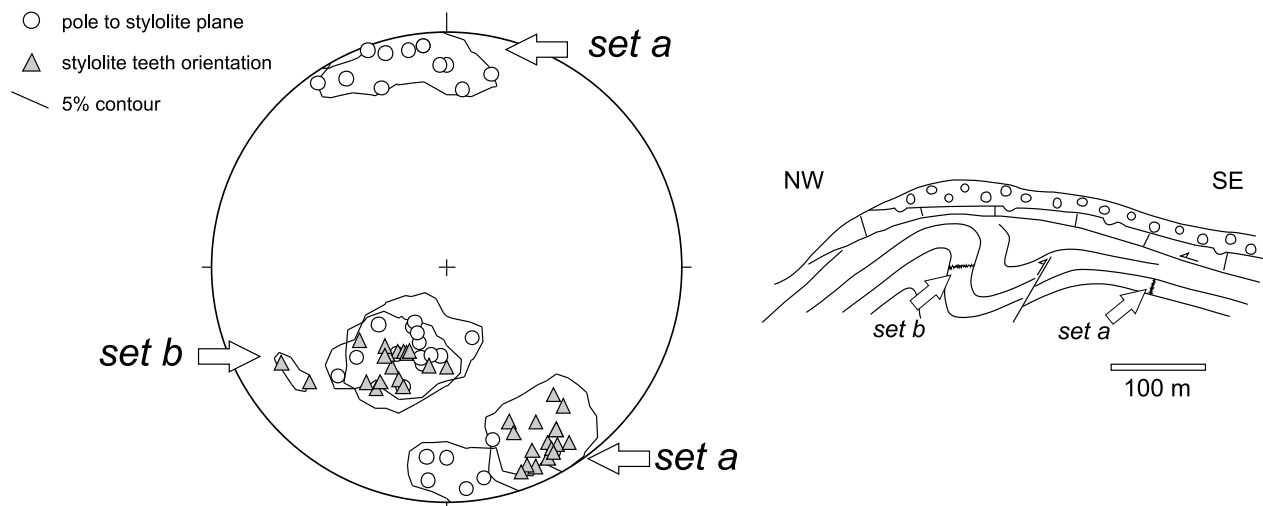


Figure 2. Lower hemispheric equal area projection (Schmidt's net) of the field data and schematic cross sections of the investigated outcrops. (a) The Swabian Alb of southern Germany ($n = 22$). The sketch at the right shows the flat-lying Jurassic strata with vertical stylolites limited to individual beds. (b) The Iberian Chain of northeastern Spain ($n = 32$). The sketch at the right shows a cross section of NE-plunging fold and the positions of sets a and b within the fold. All samples are taken from well-bedded Jurassic strata. In the overlying massif Jurassic limestones (vertical lines) and conglomerates (circles), no stylolites were found. Note that in Figure 2a, only the poles to the stylolite planes are displayed since the shortening direction is normal to that plane. In Figure 2b two populations are shown, which correspond to the two investigated fold limbs. Poles to planes (circles) diverge slightly from the orientation of the long axis of the teeth (triangle). See text for a detailed explanation.

Gwinner, 1991]. The studied sections are located 10 km south of the city of Tübingen and comprise upper Jurassic (Oxfordian to Kimmeridgian) limestones. The basal part of the sections (UTM 32U, E 0515212 m, N 5362240 m) are made up of well-bedded Oxfordian limestones, whereas the upper part of the profile contains massive Kimmeridgian limestones representing a riff facies, with sponges and algae being the main rock-forming species [Etzold *et al.*, 1996; Geyer and Gwinner, 1991]. The bedding is (sub-)horizontal, dipping slightly ($<5^\circ$) to the SE on a regional scale. The principal structural features are ENE-WSW-striking graben

structures, which exhibit a mixed-mode displacement, with a major normal and a subordinate dextral component [Etzold *et al.*, 1996; Geyer and Gwinner, 1991], and can be attributed to a later compressional phase (see below). The investigated stylolites (samples Sa6/1a, Sa6/1b, and Sa9/2) form vertical planes that trend WNW-ESE with teeth pointing parallel to the surface normal direction, hence recording a NNE-SSW compression (Figure 2a). Additionally, small-scale reverse faults and NNE-SSW-trending joints confirm the same kinematic framework. A younger subordinate set of stylolites not investigated in this study

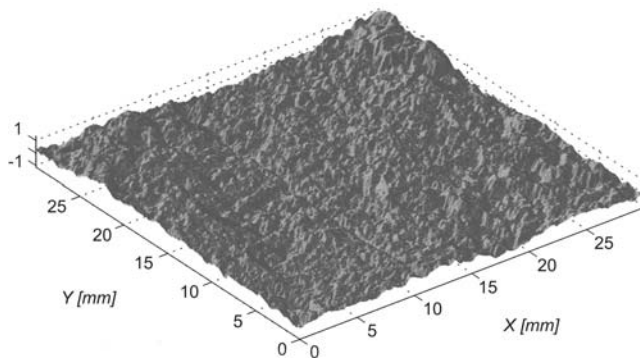


Figure 3. Oblique view of the three-dimensional (3-D) morphology of the surface of an opened stylolite (sample M4/4) reconstructed from optical profilometry. A linear trend is removed from the raw data (compare Figure 4 for details).

form NE-SW-trending vertical stylolite planes that can be related to the prominent dextral graben structures found in the area [Geyer and Gwinner, 1991; Kley and Voigt, 2008]. Our relative chronological sequence of deformation events is in agreement with data reported by Kley and Voigt [2008] demonstrating a change in the stress field from NNE-SSW-directed compression in the late Cretaceous to NW-SE-directed compression in the Neogene. This second compression phase altered neither the shape nor the orientation of the investigated stylolites, since layer parallel shortening did not cause any orientational change and deformation was restricted to stylolite interfaces.

[8] The Iberian Chain of northeastern Spain is located south of the Ebro Basin and trends roughly NW-SE. The succession is composed of up to 6000 m of Mesozoic, mainly Jurassic and Cretaceous, sediments [Capote et al., 2002], although the sequence is significantly reduced, to only 300–400 m, in the investigated area. The investigated area belongs to the Maestrazgo structural domain that forms the transition zone between the NW-SE-striking fold and thrust belt of the Aragon Branch and the NE-SW-striking Catalanian Coastal Ranges. A regional NNW-SSE compression in the sampling area between the small towns of Molinos and Ejulve is indicated by ENE-WSW-striking, 100–1000 m-scale fold trains with the top to the NNW kinematics. The onset of deformation is estimated to be around the Early to Middle Eocene, whereas the deformational peak is assumed to be during the Oligocene [Capote et al., 2002; Casas et al., 2000; Liesa and Simón, 2009]. Liesa and Simón [2009] report stylolite data that they argue to be attributed to Betic and Guadarrama compressions, both having their deformational peaks during the Oligocene. The investigated section (UTM 30T, E 07111963 m, N 4518336 m) comprises well-bedded limestones in an upper Jurassic upright antiform containing several smaller synforms that plunges 25° to the NW. Stylolites were investigated in a shallow ENE-dipping limb (set A in Figure 2b) and an overturned limb that dips steeply to the SE (set B in Figure 2b). In the eastward-dipping limb of the fold the stylolites (samples M4/1, M4/2, M4/3, and M4/4) track the far-field shortening direction (SSE-NNW) confirmed by field measurements in other outcrops in the area. In the overturned

and steeply dipping fold limb the stylolites (samples M4c/1 and M4c/3) are rotated around the fold axis into a shallow dipping orientation (i.e., a counterclockwise or clockwise rotation of 65° around the fold axis would transform the stylolite orientation from one limb into the orientation of the stylolites in the other limb of the fold). Hence, the stylolite formation in this outcrop predates the folding event. In addition, the angle between the stylolite plane and the bedding (not shown) is consistent in both positions of the fold, thus corroborating the evidence that stylolitization predates the folding event. It must be noted that stylolites in sets A and B both form in a vertical orientation. Another important feature is that the stylolite teeth are somewhat oblique (~10°) to the mean stylolite plane, which we interpret as a result of a pressure-solution overprint of a pre-existing joint set that strikes NE-SW, subparallel to the stylolite planes.

3. Methodology

[9] The samples collected in the locations described above were all taken oriented in the outcrop to reconstruct the spatial position of the 3-D stylolite morphology after laser profilometry. For analysis, only “closed” specimens were considered. Stylolite surfaces that were already open in the outcrop and were subjected to an unknown amount of weathering were ignored. The sampled specimens were opened mechanically along the two opposing interfaces of the stylolite. This method causes some negligible damage to the surface due to the interlocking of asperities. The split surfaces were cleaned from any clay material, that is, the residuum of the dissolved rock, with a soft brush and distilled water. Areas that did not exhibit visual mechanical damage were chosen for profilometry.

[10] Optical profilometry is based on a laser triangulation of the surface similarly to previous studies [Renard et al., 2004; Schmittbuhl et al., 2004, 2008]. The triangulation technique uses a laser beam that is focused on the surface of the object, which is monitored by a nearby CCD sensor. The distance between the object and the sensor changes as a function of changes of the angle under which the point of consideration is observed. The distance between the object and the laser head is then calculated from angular relationships [Schmittbuhl et al., 2008]. Before every individual measurement a test run was made to calibrate voltage fluctuations of the laser beam (the volt-height relationship is virtually linear in the chosen range, which gives the estimate of the vertical resolution: small distortions of the profile height, <1%, can be expected.). The laser beam is 30 μm wide and horizontal steps between measurement points were Δx = Δy = 25 μm, with a horizontal precision of 1 μm. The vertical resolution is 2 μm. Maps were constructed by movement of the laser head along parallel profiles over the specimen (Figure 3). Eight samples have been measured at a high resolution (Δx = Δy = 25 μm), with map sizes of 1200 × 1200 (samples M4/1 and M4/4), 1600 × 1600 (samples Sa6/1a, Sa6/1b, M4/2, M4/3, M4c/1, and M4c/3), and 2000 × 2000 measurement points (sample Sa9/2), which correspond to square maps with physical side lengths of 30, 40, and 50 mm. The x and y directions are arbitrary choices parallel to the principal axis of the profilometer. The sample is usually oriented in a way to fit the biggest square

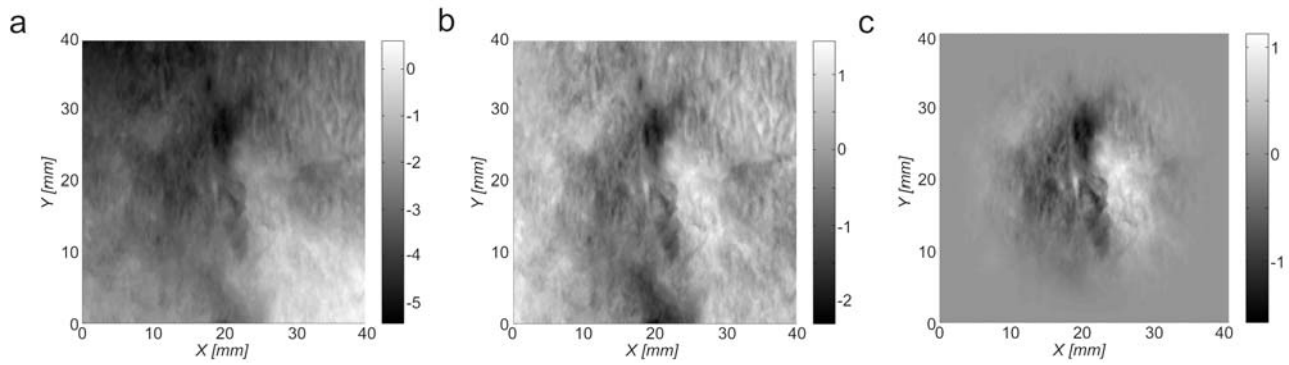


Figure 4. Grayscale maps of sample M4/3: (a) raw data from profilometry (notice a general trend from the top left to the bottom right); (b) detrended data, i.e., the linear trend is removed and the mean height is set to be zero; (c) detrended data modified with a Hanning window technique where the data are forced to taper off to zero at the boundaries (for explanation see text). Light colors correspond to peaks and ridges, and dark colors represent local depressions.

map on the respective stylolite interface. Care was taken that from the orientation of the map x/y direction, the sample orientation could be reconstructed.

[11] Additionally, sample Sa6/1 was measured twice, where the second measurement (Sa6/1b) was rotated 32° clockwise around a vertical axis with respect to the first measurement (Sa6/1a). This was done to test the robustness of the measurements used against possible noise arising from the measurement procedure along discrete profiles. An image registration [Goshtasby, 1986, 1988] of the two measurements in the spatial domain revealed the same amount of rotation, 32° , with an uncorrelated noise in the height difference between the two maps (not shown). This height difference is less than 5% (i.e., the ratio of the standard deviation σ of the height difference to the σ of the height of the surface is $0.063/1.477$ mm). Hence, there seems to be no significant error introduced by the measurement procedure.

4. Data Analysis

[12] Before we analyzed the 2-D maps in detail the raw data from the laser profilometry were subjected to a series of pretreatments (Figure 4). First, a mean plane calculated from a least-squares fit was subtracted from the raw data (Figure 4a); that is, the x/y plane was adjusted to a global trend and the vertical (z) axis was set to have zero mean height (Figure 4b). To increase the quality of our Fourier transforms (described below), we used a Hanning window technique [Karcz and Scholz, 2003; Press et al., 2007] to force our data to taper to zero at the boundaries (Figure 4c), to reduce spectral leakage (compare Figure 3). This is a standard technique in signal processing, which does not modify the frequency or amplitude of the original signal.

4.1. One-Dimensional Analysis

[13] From the 2-D height field a 1-D profile can be extracted either along the x or y direction or in any arbitrary direction. For an arbitrary 1-D profile $f(x)$ the Fourier transform $F(k)$ can be calculated and the power spectrum $P(k) \sim |F(k)|^2$ of the transform can be plotted as a function of the wave number $k = 2\pi/\lambda$ (m^{-1}), which scales inversely to

the wavelength λ [Renard et al., 2004; Schmittbuhl et al., 1995, 2004]. In Figure 5 the averaged spectra of sample M4/3 along the x and y directions of the measured map are shown. The averaged spectra are found by calculating the mean $P(k)$ for every k value over all k profiles in one direction [Renard et al., 2004; Schmittbuhl et al., 2004]. This averaging procedure reduces the noise attached to an individual 1-D profile. A linear slope of the power spectra confirms a self-affine scaling invariance. The power spectrum of a self-affine signal behaves as

$$P(k) \sim k^{-D-2H}, \quad (2)$$

where D is the topological dimension of the signal ($D = 1$ for 1-D profiles) and H is the Hurst exponent. The Hurst exponent can thus be calculated from the slope of the power spectra. When we study the averaged 1-D spectra of a tectonic stylolite along specific directions (Figure 5a), we see that the signal exhibits two slopes, which are separated by a crossover length (L) in agreement with observations on bedding parallel stylolites [Ebner et al., 2009b; Renard et al., 2004; Schmittbuhl et al., 2004]. The two observed scaling regimes have typical Hurst exponents of $H_S \sim 0.5$ and $H_L \sim 1.1$ for the small and large scale (large and small wave number), respectively. These observations indicate that the scaling of bedding parallel stylolites [equation (1)] can be extended to tectonic stylolites (compare Figure 5a). To enable a more detailed comparison of the power spectra of our tectonic stylolites from two different (orthogonal) directions, we normalize the power spectra along the x direction with the power spectrum of the y direction at $k = 1$ (mm^{-1}), that is, $P_x(k)/P_y[1$ (mm^{-1})] as shown in the inset to Figure 5a. This normalization yields a collapse of the large k values (small scales), but a notable difference for the small k values (large scales), of the scaling functions. This is basically the expression of the shift in cutoff between the two linear subbranches, which is the crossover length L . Figure 5b shows that the calculated cutoff between the scaling regimes and thus the crossover length differ between them. With 1.22 and 0.62 mm for the x and y directions, the crossover length changes by 0.6 mm (Figure 5b). The nonlinear fitting, shown by the solid line in both plots in

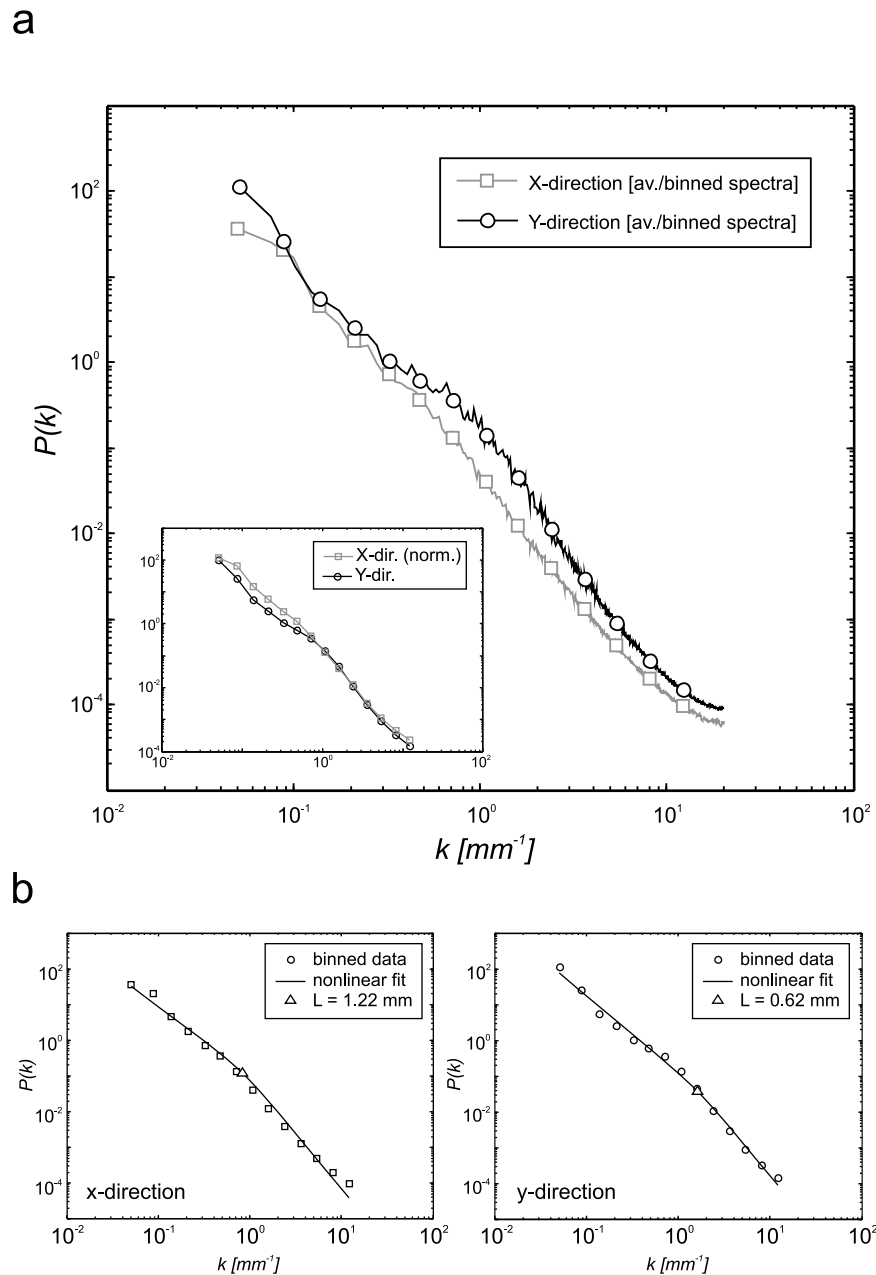


Figure 5. One-dimensional data analysis of sample M4/3. (a) Averaged power spectra $P(k)$ (solid line) and the respective binned spectra (circles) plotted as a function of the wave number along the x and the y direction of the measured map. The inset in (a) again shows the power spectra for both directions but the x direction is now normalized with respect to the y direction, $P_x(k)/P_y(1 \text{ mm}^{-1})$. This yields a collapse of the large k values (small scales). Note that for the small k values (large scales), the scaling functions deviate considerably. (b) Nonlinear fit of the binned spectra for both directions used to estimate the cross-over length L (triangle). Along the x direction the crossover length is larger ($L = 1.22$) than along the y direction ($L = 0.62$). The slope of the branches of the nonlinear model corresponds to Hurst exponents of 1.1 and 0.5 for small and large scales, respectively.

Figure 5b, is a linear-by-parts least-squares fit in logarithmic space with a weighting function that changes from the small-scale to the large-scale fraction of the scaling law (for details compare *Ebner et al.* [2009b]). This nonlinear model uses a minimization algorithm to find the least-squares fit for the crossover length. The differences found between the two directions also include a discrepancy in the scaling

prefactor, that is, a vertical shift of the power spectra, which is clearly higher for all scales in the y direction.

[14] To fully quantify rough surfaces it is necessary to characterize this prefactor of the scaling function and thus obtain a full description of the surface morphology. In the following we use the height-height correlation function to calculate the scaling prefactor. The height-height correlation

function [Barabasi and Stanley, 1995] is defined for a function $h(x)$ over the spatial variable x by $C(\Delta x) = [\langle (h(x) - h(x + \Delta x))^2 \rangle]^{1/2}$, where $\langle \rangle$ denotes the average over the range of x , which estimates the average height difference between two points in the profile separated by a distance Δx . For a self-affine profile the correlation function follows a power

law such that $C(\Delta x) \sim t^{1-H} \Delta x^H$, where H is the Hurst exponent and t is the scaling prefactor. The prefactor can be designed as $C(t) = t$ and, thus, denotes a length scale, also known as the topothesy [Renard et al., 2006; Schmittbuhl et al., 2008; Simonsen et al., 2000]. The topothesy corresponds physically to the length scale for which the slope of the rough profile is equal to 1. In other words, t is the theoretical length scale over which the rough profile has a mean slope of 45°. The smaller the t , the flatter the profile appears on a macroscopic scale.

[15] Figure 6a shows a scaling of the correlation function with two linear subbranches separated by a crossover length similar to the scaling of the power spectra shown in Figure 5a, with only the slopes being different. The correlation function shows, similarly to the power spectra, two linear subbranches separated by a distinct crossover length. We use the same nonlinear fitting approach as described previously (with fixed Hurst exponents of 0.6 and 0.3). The different scaling exponents compared to the power spectral approach is in line with the reliability of self-affine measurements performed on synthetic signals [Candela et al., 2009; Schmittbuhl et al., 1995]. Those authors have demonstrated that the correlation function underestimates the input Hurst exponents and thus shows lower values than the power spectra. The scaling prefactor and thus the topothesies t_s and t_l for the small- and large-scale regimes can be found by intersection of the two subbranches of the scaling function with the 1/1 line (Figure 6a). We estimated the topothesy for all orientations on the surfaces (Figures 6b and 6c) and found that there is a weak anisotropy in the scaling prefactor, which shows a correlation, with the highest topothesies being parallel to the horizontal direction in the sample orientation (Figure 6b) for most samples, but this is only visible in the small-scale regime. This observation is similar to what we found from investigation of the power spectra, where the small-scale regime shows very consistent results but the large-scale regime reveals a higher degree of variability; for example, compare the inset in Figure 5a. The small-scale topothesy is shown in Figure 6c. The average topothesies range between 0.05 and 0.15 mm and between 0.15 and 0.3 mm for the small and large scales, respectively.

[16] Both the power spectra (i.e., the cutoff length between the linear subbranches) and the topothesy of a 1-D signal show a considerable degree of anisotropy, which is often obscured owing to the noise associated with an individual

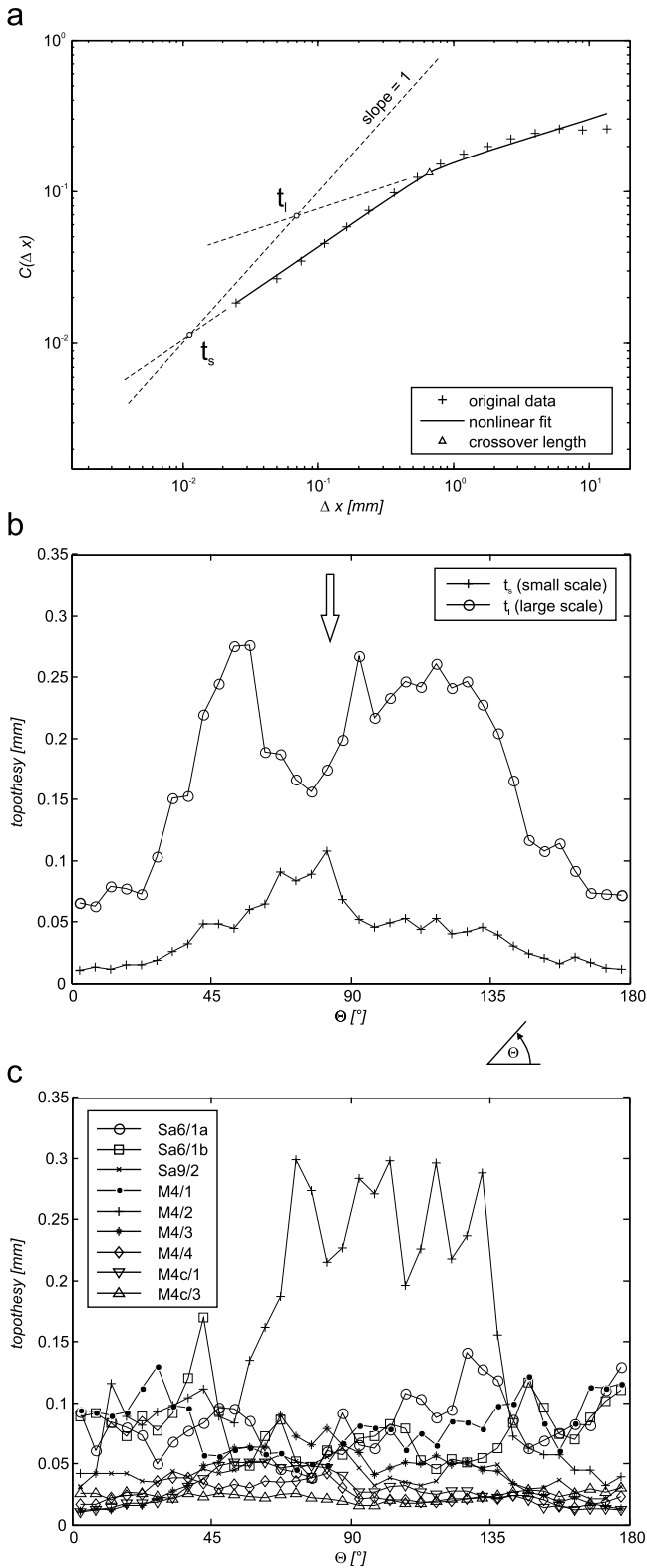


Figure 6. One-dimensional analysis of the scaling prefactor, i.e., the topothesy of tectonic stylolites. (a) A loglog plot of the correlation function $C(\Delta x)$ of a 1-D slice of sample M4/3 oriented parallel to the x direction of the analyzed surface with the nonlinear fit (compare text for details) and the topothesies t_s and t_l for small and large scale subbranches. The topothesy is constructed from the intersection of the linear subbranches with the 1/1 line. (b) The topothesies t_s and t_l of sample M4/3 plotted as a function of Θ , i.e., the counterclockwise angle from the x direction of the map. Note that the correlation functions are averaged over 5° intervals. The arrow indicates the vertical direction projected onto the stylolite plane. Note that only the t_s shows a clear correlation with the sample orientation. (c) The small-scale topothesy t_s for all samples plotted as a function of Θ .

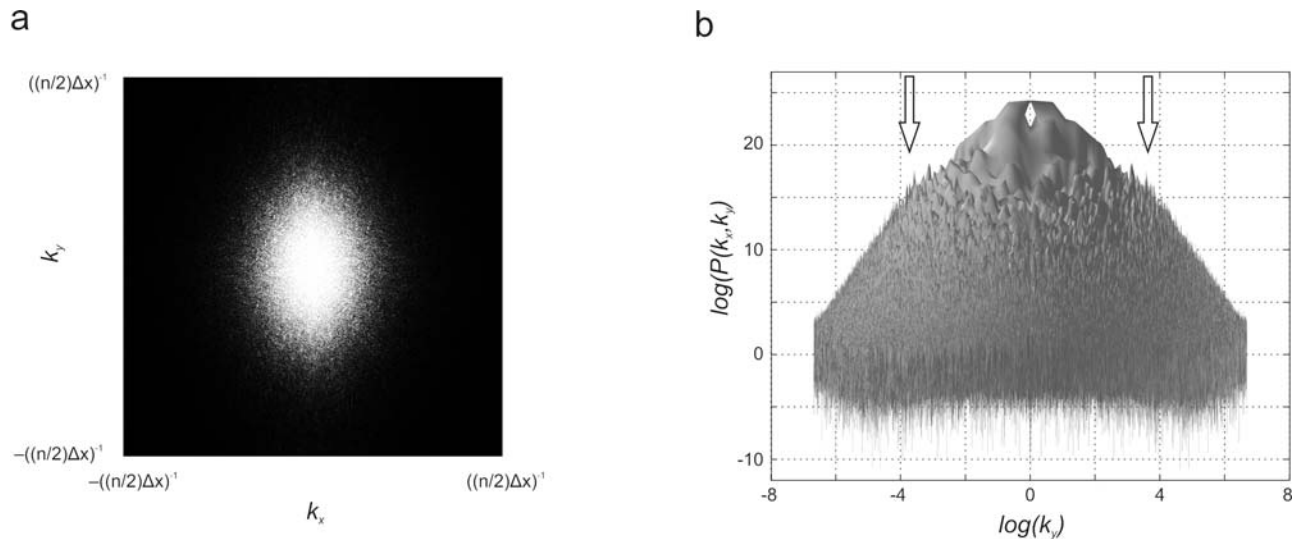


Figure 7. Two-dimensional data analysis of sample M4/3. (a) Two-dimensional Fourier transform plotted on a regular grid as a function of k_x and k_y , which range from $-[(n/2)\Delta x]^{-1}$ to $[(n/2)\Delta x]^{-1}$, where n is the number of measurement points in one direction of the map and Δx is the step size. Note that the zero-frequency component lies in the center of the map. A clear anisotropy of the data can be observed sub-parallel to the k_y axis (vertical axis). To investigate the power-law scaling exhibited by the 1-D analysis, the 2-D Fourier transform is converted to a double-log space, where $\log(k_x, k_y)$ is plotted as a function of the logarithm of the power spectra. (b) The 2-D power spectra are plotted as a surface whose height corresponds to $\log[P(k_x, k_y)]$. The 3-D surface is viewed along the k_x direction and the arrow indicates the crossover length L , which separates the two scaling regimes, i.e., the two linear subparts of the slope of the cone.

1-D profile. We conclude that to account for this in-plane variation, a 1-D signal fails to capture all scaling characteristics of tectonic stylolites and the choice of the investigated profile is not arbitrary as for bedding parallel stylolites. Hence, tectonic stylolites have a measurable in-plane anisotropy that we want to characterize in detail with a 2-D approach.

4.2. Two-Dimensional Analysis

[17] For the 2-D analysis we used the processed data as described at the beginning of this section (Figure 4c). First, a 2-D Fourier transform, that is, a discrete Fourier transform (DFT) was calculated from the data points of the 2-D height field with the fast Fourier transform algorithm [Cooley and Tukey, 1965] implemented in Matlab. Then the discrete Fourier transform is shifted so that the zero-frequency component lies in the center of the spectra and the 2-D power spectrum $P(k_x, k_y)$ is again calculated as the square of the absolute magnitude of the Fourier transform. Figure 7a displays a map of the 2-D power spectra $P(k_x, k_y)$ in which the absolute magnitude squared is shown as grayscale values and k_x and k_y range from $-[(n/2) \times \Delta x]^{-1}$ to $[(n/2) \times \Delta x]^{-1}$, where n is the number of measurement points in one direction of the map and $\Delta x = \Delta y$ is the step size. To investigate the power-law behavior located in the 1-D signals, the 2-D power spectra had to be transformed to a double-logarithmic space originating from the center of the map, that is, the zero-frequency component or the smallest wave number. This is accomplished by translating every value pair (k_x, k_y) by $\log\left(\sqrt{k_x^2 + k_y^2}\right)$ along the direction

defined by the direction cosine of the position vector (k_x, k_y) with the x axis of the coordinate system and plotting $\log[P(k_x, k_y)]$ on the newly formed logarithmic grid. The central point in this case corresponds to the system size, which imposes the smallest nonzero k . Figure 7b illustrates such a double-log plot of sample M3/4, in which the power spectra are displayed as a 3-D surface. Note that the view direction is along the k_x axis. The slopes of the surface, which roughly describe an elliptical cone, clearly exhibit two linear branches and a distinct crossover region (L) marked by the arrow in Figure 7b. Thus the 3-D representation is consistent with the scaling behavior found from the analysis of the 1-D signal.

[18] For further analysis of the anisotropy we resample the 3-D representation (Figure 7b) with a 2-D logarithmic binning (along k_x and k_y direction), to get a constant density of grid points in double-logarithmic representation (Figure 8a). For this reason a fixed grid that covers the 2-D power spectra with a constant bin size (bs) in logarithmic space [$\log(bs) = 0.4$] in the x and y direction is used to find all k_x, k_y -value pairs that fall into a certain bin, and the mean of all power spectra that belong to these k_x, k_y -value pairs in this bin is then used to define the binned power spectrum. This procedure allows analysis of the data with equal importance for the large and small scales, respectively. In addition, this method smoothes the data by removing the local fluctuations without altering the overall geometry of the 3-D representation that is characterized by the two scaling regimes and the distinct crossover.

[19] We use isopach/contour maps of the binned 2-D power spectra to quantify the degree of anisotropy. Isotropic

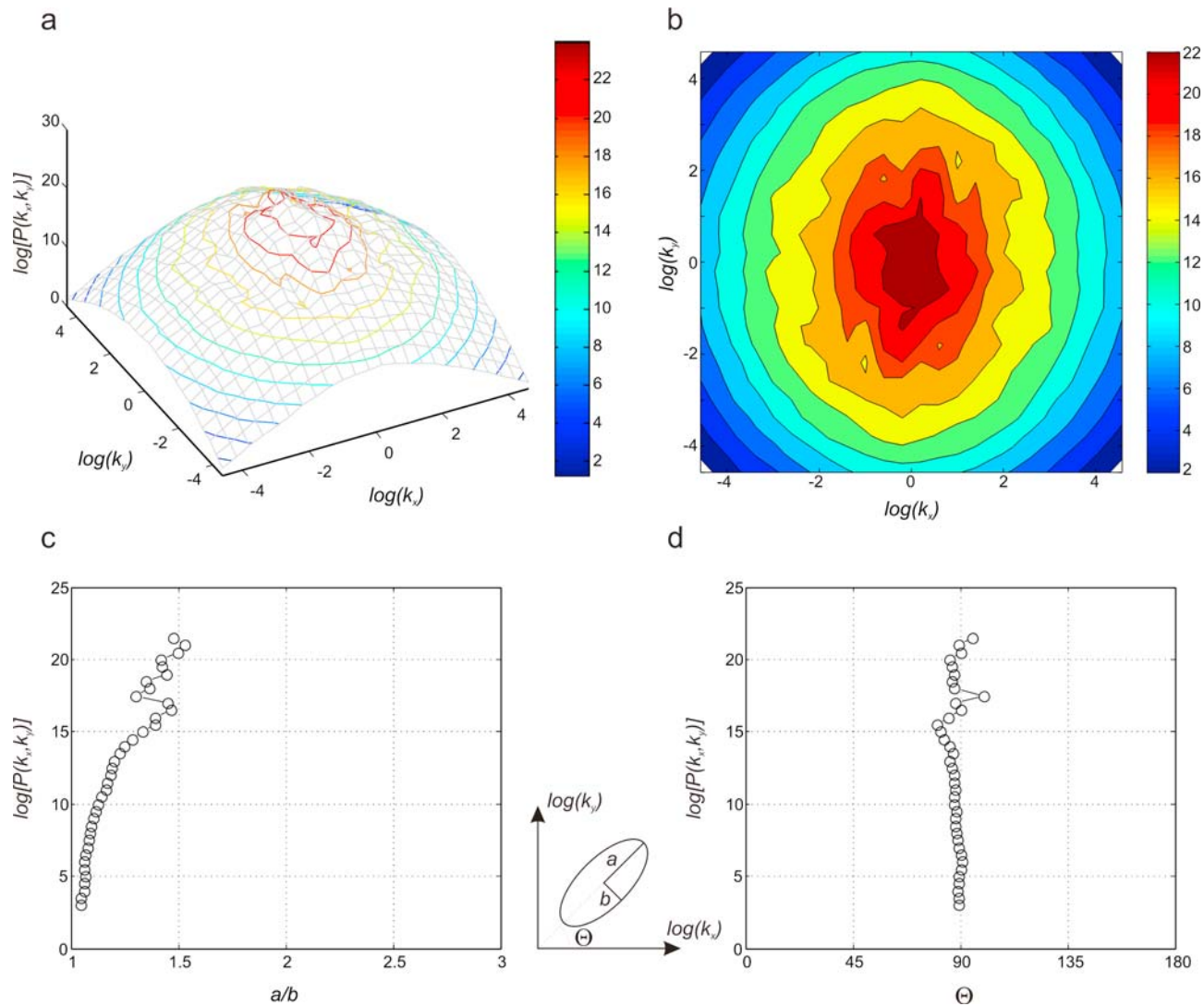


Figure 8. Quantification of the 2-D scaling anisotropy of sample M4/3. (a) Oblique 3-D view of the binned 2-D power spectra (gray mesh) with an overlay of colored contour lines of constant $\log[P(k_x, k_y)]$ values. (b) Map view of the contours calculated from the conic 2-D power spectra. These contours were utilized to calculate best-fitting ellipses using a least-squares approach. (c) Aspect ratio (a/b) of the fitted ellipse for every $\log[P(k_x, k_y)]$ contour. An increasing aspect ratio toward the center of the map is characteristic for all samples investigated. (d) Slope (i.e., the counterclockwise angle from the x direction of the measured map) of the long axis of the fitted ellipse plotted for the contour intervals.

signals should reveal concentric circular contour lines, which define the same $\log[P(k_x, k_y)]$ value. Concentric circular contour lines would imply that the crossover lengths that separate the self-affine scaling regimes for small and large scales are the same in every direction. Figures 8 show that this is clearly not the case for tectonic stylolites (also compare Figure 7a), where the contour lines reveal an elliptical shape (Figures 8a and 8b). This shape is clearly different from the circular concentric contours found in bedding parallel stylolites [compare, e.g., to Figure 4 of Schmittbuhl *et al.*, 2004]. We use a least-squares criterion to estimate the best-fit ellipse of the individual contour lines. From the best-fit ellipse we calculate the aspect ratio of the principal axis (i.e., a/b ; where a and b are the semimajor and semiminor axis of the best fit ellipse) to get a quantitative

measure of the anisotropy of the 2-D binned power spectra (Figure 8c). For the direction of the anisotropy we utilize the angle Θ between the long axis (a) of the fitted ellipse and the x direction of the coordinate system (Figure 8d). For all investigated samples we recognized an increased ellipticity toward the center of the 2-D power spectra but only a moderate or no significant change in orientation of the asymmetry with respect to the position in the power spectra. Note that in this representation (Figure 8a) high contour lines (small wave numbers) correspond to large physical length scales, whereas low contour lines (large wave numbers) correspond to small length scales.

[20] The fact that the large wave numbers display an isotropic power spectrum, that is, an aspect ratio close to 1 (Figure 8c), whereas the small ones show an anisotropic

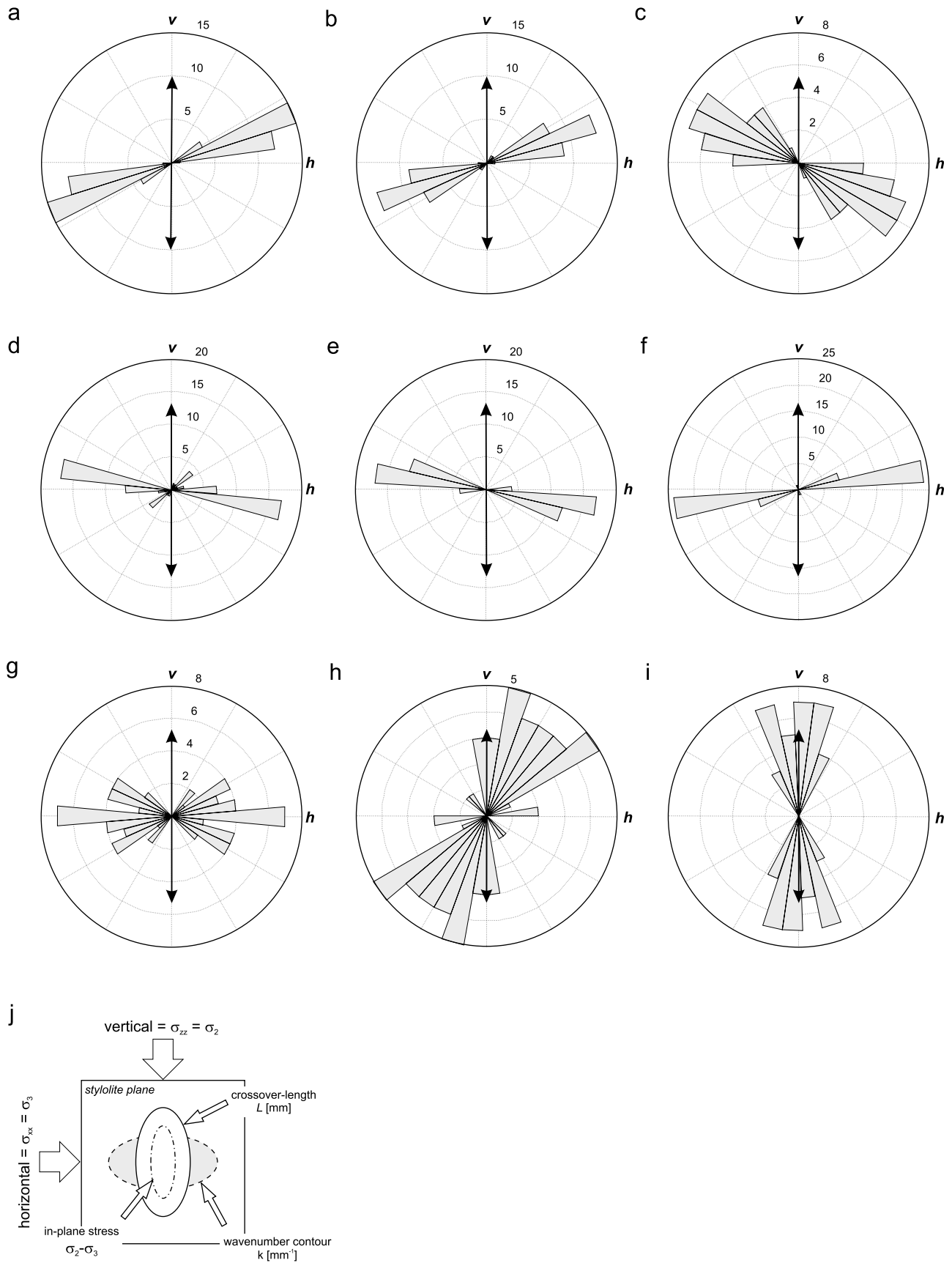


Figure 9

one, is very consistent with the result of the 1-D data analysis (see previous section). This observation is also in agreement with the physical interpretation of the mechanism of stylolite formation and morphogenesis [Ebner *et al.*, 2009b; Koehn *et al.*, 2007; Renard *et al.*, 2004; Schmittbuhl *et al.*, 2004]: At small scales (large wave numbers), the balance between surface tension and disorder controls the shape of stylolites. Both are a priori isotropic along the stylolite. In contrast, the large-scale morphologies (small wave numbers) are normally physically interpreted as resulting from a balance between the elastic field and the material disorder that controls the shape of the stylolites. The fact that an anisotropy is observed at large scales is thus the signature of an in-plane anisotropy of the stress. Since stylolite teeth are normally parallel to the largest stress direction associated with σ_1 , this large-scale anisotropy should be associated with a difference between the two principal values of the in-plane stress components, σ_2 and σ_3 .

[21] The orientation of the long axis of the fitted ellipse relative to the vertical orientation of the sample is shown in rose diagrams (Figure 9) for all samples. The long axes of the contours of the power spectrum are associated with a shorter crossover length L (i.e., reciprocal of the wave number) between the large- k isotropic scaling and the small- k anisotropic one (Figure 9j). We see in the next sections that this can be interpreted as a variation of the difference between the largest principal stress (normal to the stylolite plane) and the two in-plane stress components. The principal stress associated with the direction of the long axis should thus be the smallest one, that is, σ_3 . Arrows show the orientation of a vertical line projected onto the stylolite plane in its original outcrop orientation. From this representation (Figure 9) it is evident that the vertical direction is roughly normal to the long axis of the anisotropy for all samples except M4c/1 and M4c/3, which formed vertically (see section 2 for details) but were subsequently rotated into a shallow dipping (nonvertical) orientation plane due to folding (Figures 9h and 9i). They thus serve as a cross-check to our findings since the vertical direction in these samples does not coincide with the vertical direction during stylolite formation and the anisotropy is therefore not normal to the present vertical direction in these samples as for samples of the upright limb.

[22] To estimate the crossover length (L) and thus get quantitative information on the stresses during stylolite formation, we again use the elliptical fit as a simplified representation of the 2-D Fourier transform of our data. We assume that the crossover is located at the position of the

biggest change in the local slope of the 2-D Fourier transform (compare Figure 7b). We calculate the local slope s as the difference between the long and the short axis (a, b) of the best-fit ellipse for succeeding $\log[P(k_x, k_y)]$ contours $s = (\Delta a + \Delta b)/2$. A plot of the $\log[P(k_x, k_y)]$ contours as a function of the local slope s is shown in Figure 10a. The crossover is defined to lie at the minimum local slope in this representation and the crossover is calculated from the principal axis of the best-fit ellipse at this minimum (Figure 10b). It can be noted that the maximum crossover length coincides quite well with the vertical direction (indicated by the arrow in Figure 10b); this is in agreement with our previous observations that the anisotropy of the power spectra is also oriented (normal) with respect to the sample vertical orientation (compare Figure 9).

[23] Before we discuss the orientation of the anisotropy and the determined crossover length scales in relation to the stress tensor that was present during stylolite growth, we investigate the influence of tilted teeth on the scaling results.

4.3. Synthetic Data Analysis

[24] It is important to prove that the large-scale anisotropy we found in the investigated samples is really related to the stress field during formation and thus exclude the influence of other factors that might also cause a scaling anisotropy. The second important characteristic of tectonic stylolites, as stated in the Introduction, is the occurrence of inclined teeth, that is, slickolites. It is easy to imagine that the ridge and groove morphology of slickolites with highly inclined teeth can cause a difference in the scaling parallel or transverse to these elongated morphological features and, thus, an anisotropy. To systematically investigate the influence of a tilt of the asperities or teeth, we construct synthetic isotropic self-affine surfaces and tilt the teeth around one arbitrary axis. Tilted or inclined asperities are a common feature of slickolites [Simon, 2007] and it is commonly assumed that these structures formed when a stylolite overprinted a pre-existing plane of anisotropy in the host rock. In this case the principal stresses are oriented oblique to the pressure solution surface, which was recently proven numerically by Koehn *et al.* [2007]. Synthetic self-affine surfaces can be created following the approaches found in the literature [Meheust and Schmittbuhl, 2001; Turcotte, 1997]. We follow the method described by Meheust and Schmittbuhl [2001], who construct square white-noise maps of size $n = 512$. The self-affine correlation is then introduced by multiplying the modulus of the 2-D Fourier transform of the white noise by the modulus of the wave number raised to the power of $-1 - H$, where H is the roughness exponent.

Figure 9. Rose diagrams of all samples, i.e., a histogram with a constant bin size of 10° plotting the relative orientation of the long axis of the fitted ellipse to the vertical direction of each sample. The arrow in each diagram shows the intersection of the vertical direction of the oriented sample with the mean stylolite plane. (a) Sample Sa6/1a; (b) sample Sa6/1b; (c) sample Sa9/2; (d) sample M4/1; (e) sample M4/2; (f) sample M4/3; (g) sample M4/4; (h) sample M4c/1; (i) sample M4c/3. Note that for all samples the long axis and thus the direction with the smallest crossover length is roughly normal to the vertical direction (except for Figures 8h and 8i; for explanation see text). This direction corresponds typically to the largest differential stress, which is also the smallest in-plane stress. v and h correspond to the vertical and horizontal directions, respectively. (j) Schematic drawing of the relationship among the wave number contour (mm^{-1}) (compare Figure 8), the crossover length L (mm), the principal in-plane stresses, and the sample orientation i.e., horizontal and vertical direction. Refer to text for detailed explanation.

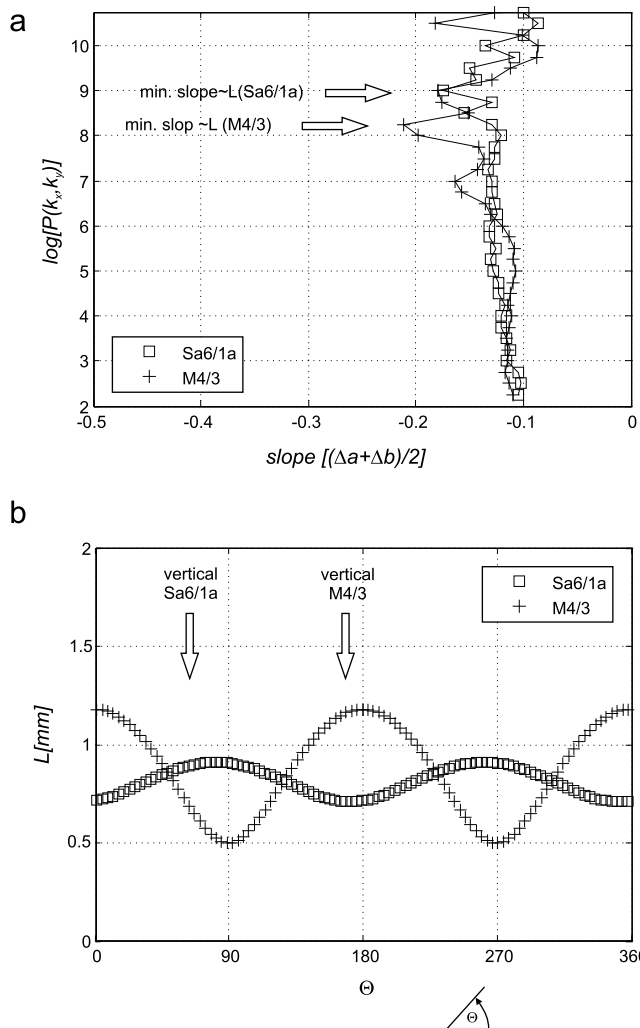


Figure 10. Crossover length from the contour data of the maps for sample M4/3 and Sa6/1a. (a) Slope of the 2-D power spectra calculated as the mean difference between the principal axis of the fitted ellipse (a , b). The biggest change in slope (arrow) is assumed to be the contour at which the crossover is located. (b) The crossover length plotted as a function of the counterclockwise angle from the x direction of the measured map. The vertical direction in the stylolite plane is indicated for both samples and roughly corresponds to the largest crossover length, i.e., the smallest differential stress as shown in Figure 1.

The self-affine surface is obtained from the inverse Fourier transform. The synthetic surface shown in Figure 11a is constructed with a Hurst exponent of $H = 0.5$ and its 2-D Fourier transform has a true isotropic self-affine behavior (compare inset in Figure 11a). A predefined tilt of the roughness is then attained from adding a linear trend along the x axis of the map, which corresponds to a tilt angle α and a subsequent back-rotation around α , that is, multiplying the data with a 3-D rotation matrix of $-\alpha$. Various tilt angles ranging from 1° to 50° were realized from the map shown in Figure 11a. To analyze single-valued functions (with no overhangs), the tilted surfaces are projected on a plane

defined by the mean surface. The data were then analyzed as described in section 4.2. The degree (aspect ratio) and orientation (slope) of the anisotropy are displayed in Figures 11b and 11c. It is evident that the original data set is isotropic, with aspect ratios for $\log[P(k_x, k_y)]$ contours close to 1. With small tilt angles, $\alpha < 10^\circ$, an anisotropy for the low $\log[P(k_x, k_y)]$ contours, and thus large wave numbers and small scales exists, which decreases with increasing α . In addition, there is a general increase in the anisotropy in all scales with tilt angles of $\alpha \geq 20^\circ$ (Figure 11b), whereas the orientation is more and more aligned with the rotation/tilt axis (Figure 11c) with increasing tilt angle. The topography of the synthetic surfaces does not exhibit a directional anisotropy but reveals a general decrease in the average topography with increasing tilt angle, from $t \sim 0.22$ for the original data down to $t \sim 0.09$ for a tilt angle of 50° .

5. Discussion

[25] We have shown that the tectonic stylolites investigated in this study, that is, stylolites that form when the principal compressive stress direction is horizontal, differ fundamentally from bedding parallel stylolites, as they show anisotropic scaling relations. Two self-affine scaling regimes (with Hurst exponents of ~ 0.5 and ~ 1.1 for the small and large scales, respectively), which are separated by a crossover length at the millimeter scale, can be found in bedding parallel and tectonic stylolites. The crossover length L scales inversely with the formation stress $L \sim \sigma^{-2}$ for bedding parallel stylolites [Ebner *et al.*, 2009b]. The analytical solution of Schmittbuhl *et al.* [2004] relates the crossover length (L) to the stress field during stylolite formation. Their stress term is a product of mean and differential stress and can be used to calculate the stress magnitudes in addition to determining the principal stress directions. The analytical solution shows that

$$L = \frac{\gamma E}{\beta \sigma_m \sigma_d}, \quad (3)$$

where E is the Young's modulus, γ is the solid-fluid interfacial energy, $\beta = \nu(1 - 2\nu)/\pi$ is a dimensionless constant with ν the Poisson's ratio, and σ_m and σ_d are the mean and differential stresses, respectively. Since perfect confinement can be assumed (that is, uniaxial strain or zero horizontal displacement) for bedding parallel stylolites, the stresses and thus the crossover length L are independent of the orientation within the stylolite surface (Figure 1a). For a tectonic stylolite with a vertical stylolite plane, the scenario is different (Figure 1b) and it can be assumed that the in-plane stresses are dissimilar. One in-plane principal stress component should be dependent on the amount of overburden and should be oriented vertically, whereas the second stress component should have a horizontal orientation. Since the crossover length L scales inversely with the product of mean and differential stress and the mean stress should be constant, variations of the crossover should reflect variations of the differential stress $|\sigma_1 - \sigma_{\text{in-plane}}|$ [compare to Schmittbuhl *et al.*, 2004]. Therefore the crossover length has to increase from a minimum in the direction of the least principal stress σ_3 (x axis in Figure 1b), and thus the

direction of the largest differential stress $|\sigma_1 - \sigma_3|$ to a maximum in an in-plane orientation normal to this direction, which corresponds to the direction of the largest in-plane stress σ_2 (the vertical direction in Figure 1b) and the smallest differential stress $|\sigma_1 - \sigma_2|$. In conclusion, it can be assumed

that the orientations of the largest and smallest crossover lengths coincide with the vertical and horizontal direction (i.e., $\sigma_{xx} < \sigma_{zz}$), respectively.

[26] Indeed we found a scaling anisotropy in our data, which shifts the crossover length accordingly (Figure 9). The 1-D analysis (Figure 5) and the 2-D data analysis (Figures 9 and 10) reveal that the long axis of the detected anisotropy is normal to the vertical direction with a crossover length maximum in this direction, implying that σ_2 has a vertical orientation. This observation holds for both investigated areas, although there is a slight deviation of up to $\pm 10^\circ$ for some samples. Only the samples (M4c/1 and M4c/3 from the overturned fold limb) that formed vertically but experienced a passive rotation subsequently to stylolite formation due to folding (compare Figures 2B, 9H, and 9I) differ significantly. This can be explained by the fact that the stylolite formation occurred prior to folding, as can be concluded from the structural relationships in the field data (Figure 2). Thus the present orientation of the samples in the overturned fold limb does not coincide with the orientation during formation of the stylolites.

[27] We noticed a small difference ($< 10^\circ$) between the orientation of the stylolite teeth and the pole of the mean stylolite plane for the samples from northeastern Spain. This is because the stylolites overprint a pre-existing joint set that is subnormal to the principal shortening direction, which influenced stylolite formation as stated previously. To investigate the effect of the tilt of the stylolite teeth and its contribution to the observed scaling anisotropy, we used synthetic self-affine surfaces that were systematically tilted to get slickolite similar structures as explained previously (Figure 11). The effect of the tilt of the teeth with respect to the mean plane of the stylolite can be characterized by (i) an anisotropy for the large wave numbers, that is, on the scale of individual teeth or asperities for small tilt angles ($< 10^\circ$), and (ii) a general homogeneous increase in the anisotropy for all scales with an increase in the tilt angle for angles $> 10^\circ$. This anisotropy caused by the imposed tilt of the asperities differs significantly from the anisotropy of real stylolites. Therefore we conclude that the 3-D formation stress is the dominant force that influences the scaling anisotropy of the investigated samples. However, one has to

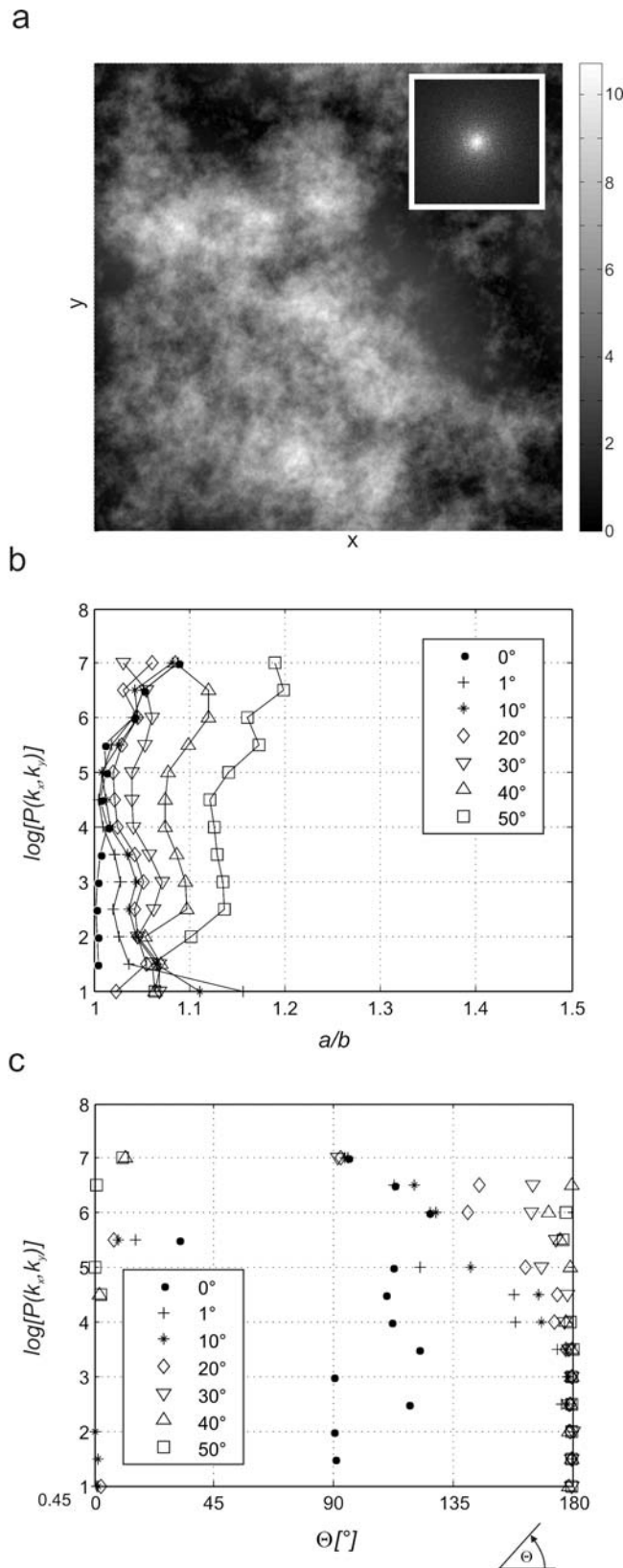


Figure 11. Grayscale map (a) of a synthetic self-affine square surface with a side length of 512 and a Hurst exponent of 0.5. Inset displays a 2-D Fourier transform of that map, which clearly exhibits isotropy with respect to its center, similar to bedding parallel stylolites. This data set is then utilized to construct slickolites, i.e., stylolites with oblique teeth and asperities (see text), with various tilt angles (e.g., 10° corresponds to oblique asperities that are rotated 10° counterclockwise around the x direction with respect to the mean plane of the synthetic surface). (b) Aspect ratio of elliptical fit of synthetic data set. For small tilt angles an anisotropy on small scales (i.e., large wave numbers and low $\log[P(k_x, k_y)]$ contours) can be observed. For large tilt angles a general increase in the aspect ratio over all scales is apparent. (c) Orientation of the long axis of the fitted ellipse (compare Figure 8d). Note the increasing alignment of the long axis of the fitted ellipse toward higher $\log[P(k_x, k_y)]$ contours with increasing tilt angles.

note that tilted teeth imply that the principal stress components are not necessarily oriented within the stylolite plane. Therefore only tectonic stylolites with plane-perpendicular teeth should be used to recalculate principal stress orientations and magnitudes.

[28] The analytical solution [Schmittbuhl *et al.*, 2004] is strictly valid only for 2-D stress cases where the principal stresses parallel to the stylolite plane are invariant along the third direction, which is truly the case for bedding parallel stylolites as discussed by Ebner *et al.* [2009b]. But since a solution for the 3-D case is not available, we argue that equation (3) could serve as an ersatz of a first approximation to calculate the order of magnitude and the difference between the principal stresses for such tectonic stresses. We assume that the crossover length in a specific direction is mainly a function of the stresses in the plane normal to the stylolite surface along the direction of investigation and that the out-of-plane stresses are invariant. This would imply that the differential stresses for the vertical and horizontal directions could be defined as $\sigma_{dv} = \sigma_{yy} - \sigma_{zz}$ and $\sigma_{dh} = \sigma_{yy} - \sigma_{xx}$, and equation (3) can be solved if the depth of stylolite formation and the material properties during stylolite formation are known. For the stylolites from the Swabian Alb, with a vertical crossover of 0.95 mm and a horizontal crossover of 0.7 mm, assuming a Poisson's ratio of 0.25, a surface free energy of calcite of 0.27 J/m², a Young's modulus of 14 GPa [Ebner *et al.*, 2009b], and a vertical stress component (σ_2) of 6 MPa (assuming a vertical load of 220 m of sediments with a density of 2.7 g/cm³, in agreement with sedimentological constraints), the tectonic stress component (σ_1) is about 17.7 MPa and the horizontal in-plane stress (σ_3) component is 1.8 MPa. See the Appendix for details of the calculation. The theoretical stresses of stylolite formation calculated here cannot serve as realistic values since we unjustifiably borrow from the analytical solution for the isotropic case but should give a first-order estimate under the limiting assumptions stated previously. Nevertheless, we would expect stresses during tectonic stylolite formation to be close to the compressive lithospheric strength, that is, $\sigma_1 - \sigma_3 \sim 14$ MPa [Banda and Cloetingh, 1992], but much smaller than the uniaxial compressive strength of laboratory measurements for limestones, which are in the range of ~ 50 – 200 MPa [Pollard and Fletcher, 2005]. Utilizing the solution given in the Appendix, the resulting stress magnitudes are surprisingly close to expected values.

[29] For our samples in Spain we do not calculate the stresses because the principal stresses are quite likely not aligned with the stylolite plane as discussed previously. We argue that even if it were possible to calculate the stresses for tectonic stylolites in a fold and thrust belt like in northeastern Spain, the stresses deduced from stylolites might be completely different form that of the folding event. The main reason is that stylolites probably form rather quickly, of the order of hundreds of years [Schmittbuhl *et al.*, 2004]. This would allow several generations of stylolites to form (revealing different finite orientations) during a single folding event; the analysis of a single set of stylolites would thus result in a snapshot from the geologic history not necessarily revealing the full picture. Even if the stylolites can be attributed to the same kinematic framework as the

folding event, both most likely have a rather diverse history in terms of stress.

6. Conclusions

[30] Vertical tectonic stylolites investigated in this study show a 1-D scaling invariance that resembles those of bedding parallel stylolites investigated in previous studies [Ebner *et al.*, 2009b; Renard *et al.*, 2004; Schmittbuhl *et al.*, 2004]. They have a self-affine scaling invariance, which is characterized by a Hurst exponent of 1.1 for long and 0.5 for short scales and a distinct crossover length at the millimeter scale that separates these two scaling regimes.

[31] High-resolution laser profilometry of tectonic stylolites provides quantitative 3-D information on these pressure solution surfaces that enables a 2-D analysis of the surface morphology. We demonstrate that our samples of tectonic stylolites have an anisotropic scaling that is not independent of the orientation of the investigated section within the plane of the stylolite. This anisotropy's main characteristic is a systematic shift of the crossover length that separates the scaling regimes. The presented analysis also confirms that the anisotropy observed in our vertical samples is oriented with respect to the horizontal and vertical direction and thus coincides with the principal stress directions within the stylolite plane for vertical stylolites, for example, σ_2 and σ_3 as depicted in Figure 2B. The long axis of the anisotropy, and thus the smallest crossover length, consistently coincides with the horizontal direction in the stylolite plane, whereas the largest crossover length is found in a vertical section. This observation is consistent with the fact that the horizontal in-plane stress is generally smaller than the vertical in-plane stress, which should be the case for tectonic stylolites (Figure 1B). They are also both smaller than the normal stress oriented perpendicular to the stylolite plane, which should be oriented horizontally. Therefore the crossover length should be smaller in a horizontal section than in a vertical section (equation (3)) using analytical considerations [Schmittbuhl *et al.*, 2004].

[32] In addition, we studied the influence of inclined teeth and asperities on the scaling behavior of stylolites. Using synthetic "slickolites" with various tilt angles, we found that the evolving anisotropy is negligible and clearly different from the anisotropy we observed in the investigated samples. We thus conclude that the scaling anisotropy of the investigated vertical tectonic stylolites can be related to the 3-D formation stress.

Appendix: Stress Calculation

Part I

[33] In this Appendix we show how the tectonic stress (σ_1) and the smaller in-plane stress component (σ_3) can be calculated if the vertical stress component can be approximated using vertical loading conditions. According to equation (A1) the vertical and horizontal crossovers (L_v and L_h) can be calculated by [Schmittbuhl *et al.*, 2004]

$$L_v = \frac{\gamma E}{\beta} \frac{1}{\sigma_m \sigma_{dv}}, \quad L_h = \frac{\gamma E}{\beta} \frac{1}{\sigma_m \sigma_{dh}}, \quad (\text{A1})$$

where E is the Young's modulus, γ is the solid-fluid interfacial energy, $\beta = \nu(1 - 2\nu)/\pi$ is a dimensionless constant with ν the Poisson's ratio, and σ_m and $\sigma_{dv/dh}$ are the mean and differential stresses, respectively. Since the mean stress is the same for both directions, we can reformulate equation (A1) to

$$\sigma_m = \frac{\gamma E}{\beta} \frac{1}{L_v \sigma_{dv}}, \quad \sigma_m = \frac{\gamma E}{\beta} \frac{1}{L_h \sigma_{dh}}, \quad (\text{A2})$$

and join both equations so that

$$L_v \sigma_{dv} = L_h \sigma_{dh}. \quad (\text{A3})$$

If we now define the differential stresses using the main principal stress components with $\sigma_1 = \sigma_{yy}$, that is, acting normal to the stylolite plane; $\sigma_2 = \sigma_{zz}$, that is, the vertical in-plane stress component; and $\sigma_3 = \sigma_{xx}$, that is, the horizontal in-plane stress component (compare Figure 1B). As $\sigma_{dv} = \sigma_{yy} - \sigma_{zz}$ and $\sigma_{dh} = \sigma_{yy} - \sigma_{xx}$, equation (A3) becomes

$$\frac{L_h}{L_v} = \frac{\sigma_{yy} - \sigma_{zz}}{\sigma_{yy} - \sigma_{xx}}, \quad (\text{A4})$$

and solving for the xx component,

$$\begin{aligned} \sigma_{yy} - \sigma_{xx} &= \frac{L_v}{L_h} (\sigma_{yy} - \sigma_{zz}), \\ \sigma_{xx} &= \sigma_{yy} - \frac{L_v}{L_h} (\sigma_{yy} - \sigma_{zz}) = \sigma_{yy} - \frac{L_v}{L_h} \sigma_{yy} + \frac{L_v}{L_h} \sigma_{zz}. \end{aligned} \quad (\text{A5})$$

Part II

[34] For simplification we substitute all material parameters in equation (A1) that are assumed to be constant, according to

$$a = \frac{\gamma E}{\beta}.$$

Then we use equation (A1) for the horizontal crossover,

$$L_h = a \frac{1}{\sigma_m \sigma_{dh}},$$

or

$$\sigma_m \sigma_{dh} = \frac{\sigma_{xx} + \sigma_{yy} + \sigma_{zz}}{3} (\sigma_{yy} - \sigma_{xx}) = \frac{a}{L_h},$$

and

$$(\sigma_{xx} + \sigma_{yy} + \sigma_{zz}) (\sigma_{yy} - \sigma_{xx}) = 3 \frac{a}{L_h}. \quad (\text{A6})$$

Now we include equation (A5) in equation (A6) and solve for σ_{yy} ,

$$\left(2\sigma_{yy} + \sigma_{zz} - \sigma_{yy} \frac{L_v}{L_h} + \sigma_{zz} \frac{L_v}{L_h} \right) \left(\sigma_{yy} \frac{L_v}{L_h} - \sigma_{zz} \frac{L_v}{L_h} \right) = 3 \frac{a}{L_h}, \quad (\text{A7})$$

and multiplying the components gives

$$\begin{aligned} 2\sigma_{yy}^2 \frac{L_v}{L_h} - \sigma_{yy}^2 \left(\frac{L_v}{L_h} \right)^2 + 2\sigma_{yy} \sigma_{zz} \left(\frac{L_v}{L_h} \right)^2 - \sigma_{yy} \sigma_{zz} \frac{L_v}{L_h} \\ - \sigma_{zz}^2 \frac{L_v}{L_h} - \sigma_{zz}^2 \left(\frac{L_v}{L_h} \right)^2 - 3 \frac{a}{L_h} = 0. \end{aligned} \quad (\text{A8})$$

Rearranging equation (A8) to solve a binomial formula gives

$$\sigma_{yy}^2 + \sigma_{yy} \frac{2\sigma_{zz} \left(\frac{L_v}{L_h} \right)^2 - \sigma_{zz} \frac{L_v}{L_h}}{2 \frac{L_v}{L_h} - \left(\frac{L_v}{L_h} \right)^2} - \frac{\sigma_{zz}^2 \frac{L_v}{L_h} - \sigma_{zz}^2 \left(\frac{L_v}{L_h} \right)^2 - 3 \frac{a}{L_h}}{2 \frac{L_v}{L_h} - \left(\frac{L_v}{L_h} \right)^2} = 0, \quad (\text{A9})$$

and the solution of the binomial formula is then

$$\begin{aligned} \sigma_{yy1,2} = -0.5 \frac{2\sigma_{zz} \left(\frac{L_v}{L_h} \right)^2 - \sigma_{zz} \frac{L_v}{L_h}}{2 \frac{L_v}{L_h} - \left(\frac{L_v}{L_h} \right)^2} \\ \pm \sqrt{0.25 \left(\frac{2\sigma_{zz} \left(\frac{L_v}{L_h} \right)^2 - \sigma_{zz} \frac{L_v}{L_h}}{2 \frac{L_v}{L_h} - \left(\frac{L_v}{L_h} \right)^2} \right)^2 - \left(\frac{-\sigma_{zz}^2 \frac{L_v}{L_h} - \sigma_{zz}^2 \left(\frac{L_v}{L_h} \right)^2 - 3 \frac{a}{L_h}}{2 \frac{L_v}{L_h} - \left(\frac{L_v}{L_h} \right)^2} \right)}. \end{aligned} \quad (\text{A10})$$

The value of σ_{xx} can be derived from equation (A5).

[35] **Acknowledgments.** J. Nebelsick, M. Maisch, O. W. Vonderschmidt, and T. Sachau are thanked for valuable discussion and support in the field. M. Ebner and D. Koehn acknowledge financial support through DFG project KO2114/5 and the MWFZ of Mainz and the Geocycles Cluster funded by the state of Rhineland-Palatinate. R. Toussaint and J. Schmittbuhl acknowledge the support of a FORPRO grant. We thank both reviewers for thorough reviews and suggestions that helped to improve the manuscript.

References

- Angheluta, L., et al. (2008), Stress-driven phase transformation and the roughening of solid-solid interfaces, *Phys. Rev. Lett.*, *100*(9), 096105, doi:10.1103/PhysRevLett.100.096105.
- Banda, E., and S. Cloetingh (1992), Europe's lithosphere—Mechanical structure, in *The European Geotraverse*, edited by D. Blundell et al., Cambridge Univ. Press, Cambridge, U.K.
- Barabasi, A. L., and H. E. Stanley (1995), *Fractal Concepts in Surface Growth*, 366 pp., Cambridge Univ. Press, Cambridge, U.K.
- Bonnetier, E., et al. (2009), Does roughening of rock-fluid-rock interfaces emerge from a stress-induced instability?, *Eur. Phys. J. B*, *67*(1), 121–131.
- Bretz, J. H. (1940), Solution cavities in the Joliet limestone of northeastern Illinois, *J. Geol.*, *48*(4), 337–384, doi:10.1086/624897.
- Brouste, A., et al. (2007), Variety of stylolites' morphologies and statistical characterization of the amount of heterogeneities in the rock, *J. Struct. Geol.*, *29*(3), 422–434, doi:10.1016/j.jsg.2006.09.014.
- Buxton, T. M., and D. F. Sibley (1981), Pressure solution features in a shallow buried limestone, *J. Sediment. Petrol.*, *51*(1), 19–26.
- Candela, T., et al. (2009), Characterization of fault roughness at various scales: Implications of three-dimensional high resolution topography measurements, *Pure Appl. Geophys.*, *166*(10/11), 1817–1851.
- Capote, R., et al. (2002), The Alpine system north of the Betic Cordillera, in *The Geology of Spain*, edited by W. Gibbons and T. Moreno, 632 pp., Geological Society of London, London.
- Casas, A. M., et al. (2000), Syn-tectonic sedimentation and thrust-and-fold kinematics at the intra-mountain Montalban Basin (northern Iberian Chain, Spain), *Geodin. Acta*, *13*(1), 1–17, doi:10.1016/S0985-3111(00)00105-4.
- Cooly, J. W., and J. W. Tukey (1965), An algorithm for machine calculation of complex Fourier series, *Math. Comput.*, *19*(90), 297, doi:10.2307/2003354.
- Drummond, C. N., and D. N. Sexton (1998), Fractal structure of stylolites, *J. Sediment. Res.*, *68*(1), 8–10.

- Dunnington, H. V. (1954), Stylolite development post-dates rock induration, *J. Sediment. Petrol.*, *24*(1), 27–49.
- Ebner, M., et al. (2009a), The influence of rock heterogeneity on the scaling properties of simulated and natural stylolites, *J. Struct. Geol.*, *31*(1), 72–82, doi:10.1016/j.jsg.2008.10.004.
- Ebner, M., et al. (2009b), Stress sensitivity of stylolite morphology, *Earth Planet. Sci. Lett.* *277*, 394–398, doi:10.1016/j.epsl.2008.11.001.
- Etzold, A., et al. (1996), Schwäbische Alb—Stratigraphie, Tektonik, Vulkanismus, Karsthydrogeologie, *Z. Geol. Wiss.*, *24*(1/2), 175–215.
- Geyer, O. F., and M. P. Gwinner (1991), *Geologie von Baden-Württemberg*, 4th ed., 482 pp., Schweizerbart'sche Verlagsbuchhandlung, Stuttgart.
- Goshtasby, A. (1986), Piecewise linear mapping functions for image registration, *Pattern Recogn.*, *19*(6), 459–466, doi:10.1016/0031-3203(86)90044-0.
- Goshtasby, A. (1988), Image registration by local approximation methods, *Image Vis. Comput.*, *6*(4), 255–261, doi:10.1016/0262-8856(88)90016-9.
- Gratier, J. P., et al. (2005), Experimental microstylolites in quartz and modeled application to natural stylolitic structures, *J. Struct. Geol.*, *27*(1), 89–100, doi:10.1016/j.jsg.2004.05.007.
- Guzzetta, G. (1984), Kinematics of stylolite formation and physics of the pressure-solution process, *Tectonophysics*, *101*(3–4), 383–394, doi:10.1016/0040-1951(84)90122-7.
- Heald, M. T. (1955), Stylolites in sandstones, *J. Geol.*, *63*(2), 101–114, doi:10.1086/626237.
- Karcz, Z., and C. H. Scholz (2003), The fractal geometry of some stylolites from the Calcare Massiccio Formation, Italy, *J. Struct. Geol.*, *25*(8), 1301–1316, doi:10.1016/S0191-8141(02)00173-6.
- Kley, J., and T. Voigt (2008), Late Cretaceous intraplate thrusting in central Europe: Effect of Africa-Iberia-Europe convergence, not Alpine collision, *Geology*, *36*(11), 839–842, doi:10.1130/G24930A.1.
- Koehn, D., et al. (2007), Growth of stylolite teeth patterns depending on normal stress and finite compaction, *Earth Planet. Sci. Lett.*, *257*(3/4), 582–595, doi:10.1016/j.epsl.2007.03.015.
- Liesa, C. L., and J. L. Simón (2009), Evolution of intraplate stress fields under multiple remote compressions: The case of the Iberian Chain (NE Spain), *Tectonophysics*, *474*(1/2), 144–159, doi:10.1016/j.tecto.2009.02.002.
- Meheust, Y., and J. Schmittbuhl (2001), Flow enhancement of a rough fracture, *Geophys. Res. Lett.*, *27*, 2989–2992.
- Park, W. C., and E. H. Schot (1968), Stylolites: Their nature and origin, *J. Sediment. Petrol.*, *38*(1), 175–191.
- Pollard, D. D., and R. C. Fletcher (2005), *Fundamentals of structural geology*, 500 pp., Cambridge Univ. Press, Cambridge, U.K.
- Press, W. H., et al. (2007), *Numerical Recipes. The Art of Scientific Computing*, 3rd ed., 1256 pp., Cambridge Univ. Press, Cambridge, U.K.
- Railsback, L. B. (1993), Lithologic controls on morphology of pressure-dissolution surfaces (stylolites and dissolution seams) in paleozoic carbonate rocks from the mideastern United States, *J. Sediment. Res.*, *63*(3), 513–522.
- Railsback, B. L., and L. M. Andrews (1995), Tectonic stylolites in the 'undeformed' Cumberland Plateau of southern Tennessee, *J. Struct. Geol.*, *17*(6), 911–915, doi:10.1016/0191-8141(94)00127-L.
- Renard, F., et al. (2004), Three-dimensional roughness of stylolites in limestones, *J. Geophys. Res.*, *109*, B03209, doi:10.1029/2003JB002555.
- Renard, F., et al. (2006), High resolution 3D laser scanner measurements of a strike-slip fault quantify its morphological anisotropy at all scales, *Geophys. Res. Lett.*, *33*, L04305, doi:10.1029/2005GL025038.
- Rutter, E. H. (1983), Pressure solution in nature, theory and experiment, *J. Geol. Soc.*, *140*(5), 725–740, doi:10.1144/gsjgs.140.5.0725.
- Schmittbuhl, J., et al. (1995), Reliability of self-affine measurements, *Phys. Rev. E*, *51*(1), 131–147, doi:10.1103/PhysRevE.51.131.
- Schmittbuhl, J., et al. (2004), Roughness of stylolites: Implications of 3D high resolution topography measurements, *Phys. Rev. Lett.*, *93*, 238501, doi:10.1103/PhysRevLett.93.238501.
- Schmittbuhl, J., et al. (2008), Fracture morphology and viscous transport, *Int. J. Rock Mech. Min. Sci.*, *45*(3), 422–430, doi:10.1016/j.ijrmmms.2007.07.007.
- Simon, J. L. (2007), Analysis of solution lineations in pebbles: Kinematical vs. dynamical approaches, *Tectonophysics*, *445*(3/4), 337–352, doi:10.1016/j.tecto.2007.09.003.
- Simonsen, I., et al. (2000), Wave scattering from self-affine surfaces, *Phys. Rev. E*, *61*(5), 5914, doi:10.1103/PhysRevE.61.5914.
- Stockdale, P. B. (1922), Stylolites: Their nature and origin, *Indiana Univ. Studies*, *9*, 1–97.
- Tada, R., and R. Siever (1989), Pressure solution during diagenesis, *Annu. Rev. Earth Planet. Sci.*, *17*, 89–118, doi:10.1146/annurev.earth.17.050189.000513.
- Turcotte, D. L. (1997), *Fractals and Chaos in Geology and Geophysics*, 2nd ed., 398 pp., Cambridge Univ. Press, Cambridge, U.K.

P. Bons, Institute for Geosciences, Eberhard Karls University Tübingen, Sigwartstr. 10, D-72076 Tübingen, Tübingen, Germany.

M. Ebner, Geological Survey of Austria, Neulinggasse 38, A-1030 Vienna, Austria. (marcus.ebner@geologie.ac.at)

D. Koehn, Tectonophysics, Institute of Geosciences, Johannes Gutenberg University, Becherweg 21, D-55128 Mainz, Germany.

J. Schmittbuhl and R. Toussaint, EOST, University of Strasbourg, Strasbourg 67081, France.